First-principles investigation of incipient ferroelectric trends of rutile TiO_2 in bulk and at the (110) surface

A. Grünebohm* and P. Entel
Faculty of Physics and CENIDE, University of Duisburg-Essen, 47048 Duisburg, Germany

C. Ederer†
Materials Theory, ETH Zürich, Wolfgang-Pauli-Str. 27, 8093 Zürich, Switzerland

(Received 21 May 2012; published 25 February 2013)

The ferroelectric trends of rutile (TiO_2) in bulk and at the (110) surface are investigated by means of *ab initio* density functional theory. We discuss the underlying mechanism of the incipient ferroelectric behavior of rutile in terms of Born effective charges, which we decompose in individual contributions by means of maximally localized Wannier functions. We show that a ferroelectric phase can be stabilized for a variety of different lattice distortions, which all enlarge the shortest Ti-O distance, even if the longer apical Ti-O bond is simultaneously shortened. At the (110) surface, the ferroelectric trends are modified compared to the bulk, but nevertheless, ferroelectric phases with large polarization even in the topmost surface layer can be stabilized by uniaxial strain.

DOI: 10.1103/PhysRevB.87.054110 PACS number(s): 77.80.bn, 77.84.Bw, 77.55.fp

I. INTRODUCTION

TiO_2 in the rutile structure has been classified as an incipient ferroelectric material, based on the experimental observation that the dielectric permittivity is exceptionally large and increases with decreasing temperature, although no ferroelectric transition occurs even for $T = 0$ K.[1–3] The realization of ferroelectric TiO_2, or even the possibility to efficiently tune its dielectric constant, would be of great technological importance, since TiO_2 is a cheap material with well optimized processing methods, which is used for a variety of applications such as optical coating,[4] solar cells,[5] or sensors.[6] Many of these applications are based on properties involving the rutile (110) surface, which is the technologically most relevant and therefore best-studied rutile surface.[7–11]

Previous theoretical *ab initio* studies have shown that in the corresponding bulk material the anomalous behavior of the dielectric constant is a consequence of a low-frequency polar (A_{2u}) phonon mode,[12] which softens under negative pressure or uniaxial tensile strain along the (001) axis.[13–15] Liu *et al.* classified the phase transition between the paraelectric and ferroelectric phases to be of second order. Since the resulting magnitude of the ionic off-centering as well as the electric polarization are in the same range as for prototypical ferroelectrics such as $PbTiO_3$ or $BaTiO_3$, an enforced ferroelectric transition would lead to a technologically relevant ferroelectric material. Furthermore, Mitev *et al.* found a large region within the Brillouin zone with a low-lying phonon branch, which may be linked to the structural relaxation of the rutile (110) surface.[16] These authors also pointed out a softening of this mode under uniaxial strain in both [001] and [110] directions and found that the ferroelectric A_{2u} mode is quite insensitive towards [110]-oriented strain. In contrast, we have shown more recently that the A_{2u} mode, indeed, also softens under [110] strain, but that a different polar mode, an E_u mode polarized along [110] becomes even more unstable than the A_{2u} mode under this strain orientation.[17] Under uniaxial tensile [110] strain, we have thus found a second-order phase transition to a ferroelectric phase with polarization along [110].[18] In agreement with these results, a softening both of the A_{2u} mode and of the lowest E_u mode has also been found in Ref. 15 for tensile uniaxial [001] strain and for an isotropic lattice expansion within the (100)/(010) plane. Since the strain dependence of the two polar modes is different, this opens up the interesting possibility to "strain engineer" the polarization direction.

It is well known that ferroelectric or dielectric properties can be significantly modified at surfaces in comparison with the corresponding bulk material. First of all, a polarization along the surface normal induces a depolarizing field, and is therefore often suppressed in thin films (see, e.g., Ref. 19). Second, the reduced coordination of the surface atoms may prevent or enhance ferroelectric trends,[20–22] as the dipolar interaction and the short-range repulsion are both modified. Finally, the surface-induced atomic relaxations can also modify the bonding and thus the ferroelectric properties. For example, it has been discussed whether the surface relaxation and the unsaturated bonds at the surface are able to destabilize the paraelectric state, leading to a finite electric polarization in the related incipient ferroelectric material $SrTiO_3$.[20,21,23] We also note that a ferroelectric transition has been observed experimentally in strained $SrTiO_3$ films.[24] Therefore an obvious approach to achieve a ferroelectric transition in rutile is the growth of strained thin TiO_2 films.

In view of this, it is essential to test the modifications of the ferroelectric properties of the strained TiO_2 (110) surface, as considerable differences may appear compared to the bulk case. Nevertheless, to the best of our knowledge, no such investigation of the ferroelectric trends of this TiO_2 surface has been undertaken until now.

In the present paper, we first present a systematic comparison of the effects of different lattice modifications on the ferroelectric properties of bulk rutile TiO_2. We show that each lattice modification that affects the nearest-neighbor Ti-O distances within the crystal can stabilize a ferroelectric phase polarized along (001). Additionally, we discuss the fundamental mechanisms for the incipient ferroelectric behavior of rutile TiO_2 in the framework of Born effective

charges. We then present the *ab initio* investigation of the ferroelectric trends of the TiO_2 rutile surface. Although we find strong surface-induced relaxations and modifications of the electronic structure, which have a considerable influence on the ferroelectric properties, the strong ferroelectric tendencies of the bulk material are essentially retained at the surface. In addition, two different ferroelectric states with polarization within the surface plane can be stabilized for strained TiO_2 films. Here, local dipoles both along (001) and along $(\bar{1}10)$ can be stabilized within the surface at 2% uniaxial strain. Furthermore, the magnitude of the polarization increases as the strain is enlarged to 5%.

This paper is organized as follows. In Sec. II, we present our computational methods and all related technical details. In Sec. III, we discuss the ferroelectric trends of bulk rutile in some detail. This is essential in order to make reliable predictions on the ferroelectric trends of the surface discussed in the later sections. For this purpose, the ferroelectric trends under different lattice modifications and a discussion of the underlying mechanisms will be presented in Secs. III B and III C, respectively. We outline the ferroelectric trends of the rutile (110) surface in Sec. IV, both in free films and for films that are clamped to an idealized substrate (see Sec. IV C). Finally, we show that different ferroelectric distortions can be stabilized in the surface under tensile uniaxial strain and discuss the resulting displacement patterns in Sec. IV D. Conclusions and outlook on future work are summarized in Sec. V.

II. COMPUTATIONAL DETAILS

The electronic structure of TiO_2 is calculated using first-principles density functional theory.[25] Most calculations are performed by employing the Vienna *ab initio* simulation package (VASP 5.2.2)[26] based on projector augmented wave pseudo-potentials.[27] Born effective charges and the dielectric permittivity are calculated within VASP using density functional perturbation theory.[28] The generalized gradient approximation (GGA) in the formulation of Perdew, Burke, and Ernzerhof (PBE)[29] is used for the exchange correlation energy and $4s3d$ $(2s2p)$ electrons are treated as valence for Ti (O). This is motivated through further studies of TiO_2-Fe heterostructures, where GGA is required to obtain good structural properties of Fe and a small number of electrons is desirable to reduce the computational effort. As shown in Ref. 13, the ferroelectric trends of TiO_2 may be overestimated by GGA potentials, and small inaccuracies may result from the use of our rather soft Ti pseudopotential.[30] However, we could not find large qualitative differences in the description of the electronic and dielectric properties within our approach compared to an enlarged valence basis set and LDA potentials[18] and thus stick to the minimal valence electron basis. In fact, as will be seen in Sec. III, excluding the Ti semicore states from the valence, slightly reduces the polarizability of the Ti cations, and thus reduces the artificial instability of the ferroelectric mode found in other GGA calculations using a larger valence. We also note that a more accurate description of the structural, electronic, and dielectric properties could be achieved by using hybrid DFT-Hartree Fock exchange correlation functionals such as HSE or B3LYP, cf. Ref. 31, but only at significantly increased computational effort.

A plane-wave cutoff of 500 eV, an energy convergence better than 10^{-7} eV, and at least $6 \times 6 \times 6$ $(5 \times 13 \times 3)$ k-points constructed with the Monkhorst-Pack[32] scheme for bulk (films) guarantee sufficient accuracy of our calculations. A Gaussian smearing of 0.1 eV is used for most calculations in order to improve the convergence with respect to the number of k-points. This smearing is reduced to 0.05 eV for the determination of the bulk Born effective charges, and the linear tetrahedron method is used for the determination of the harmonic frequencies. Atomic positions are optimized until the residual forces are smaller than 0.001 eV $Å^{-1}$ (0.005 eV $Å^{-1}$) for bulk (surface) calculations. For the surface calculations, at least 10 Å of vacuum is used between the periodic images of the films.

The plane-wave self-consistent field (PWscf) code, which is part of the QUANTUM ESPRESSO package,[33] in combination with WANNIER90,[34] is used to construct maximally localized Wannier functions (MLWFs)[35] for the orbital decomposition of the Born effective charges of bulk rutile TiO_2. For this purpose, a Γ-centered equidistant $14 \times 14 \times 20$ k-point grid, a plane-wave cutoff of 35 Ry (≈476 eV) for the wave-function (420 Ry for the charge density) and an energy convergence of 10^{-8} Ry ensure sufficient accuracy. The Ti $3s$ and $3p$ semicore states are treated as valence electrons in the PWscf calculations. For the MLWF decomposition of the surface, the k-point grid is reduced to $6 \times 12 \times 2$. MLWFs are constructed separately for valence and semicore states, based on appropriate initial projections, and the total spread is always converged better than 10^{-10} $Å^2$ $(10^{-7}$ $Å^2)$ per Wannier function for the bulk (surface).

III. BULK RUTILE

In order to provide a well-defined reference for the interpretation of our results for the TiO_2 rutile (110) surface in Sec. IV, we first discuss results for the corresponding bulk system.

A. Structural properties

The atomic structure of TiO_2 in its rutile morphology is tetragonal with $P4_2mnm$ symmetry, see Fig. 1. Besides the lattice constant a and the tetragonal c/a ratio, an internal parameter u defines the Ti-O distances. Each Ti atom is sixfold coordinated by O atoms with four short equatorial Ti-O bonds (Ti-O_{eq}), $d_{eq} = |(2u - 1, 2u - 1, c/a)|\ a/2$, and two long apical Ti-O bonds (Ti-O_{ap}), $d_{ap} = |(u, u, 0)|\ a$.

It has been shown that the ferroelectric trends of bulk rutile depend critically on the lattice parameters.[14,16–18,37] Because of this, a correct description of the atomic structure is essential. Our calculated lattice parameters, see Table I, and the calculated pressure dependence of these quantities, see Table II, fit better to experimental results than calculations based on the commonly used local density approximation (LDA). Nevertheless, the LDA error is overcorrected, leading to an overestimation of the lattice constant by 1.6% compared to low-temperature experimental results, which may also lead to a quantitative overestimation of the ferroelectric trends. We note

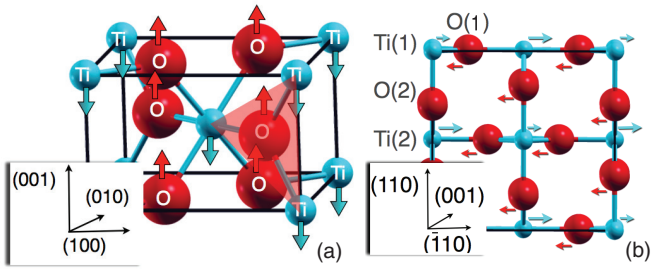

FIG. 1. (Color online) Atomic structure of rutile: Ti (blue, light) and O (red, dark). (a) Primitive unit cell. Arrows mark the atomic displacements of the A_{2u} phonon mode. The atomic structure can be decomposed into O-Ti_3 units, see red triangle. (b) $\sqrt{2} \times 1 \times \sqrt{2}$ cell in [$\bar{1}$10], [001], [110] coordinates. Ti(1)/Ti(2)/O(1)/O(2) mark symmetry-inequivalent atomic classes under [$\bar{1}$10] strain. Arrows mark the polar atomic displacements under [$\bar{1}$10] strain, see Ref. 18.

that, while an artificial destabilization of the paraelectric phase for GGA potentials has been found in Ref. 13, we could not reproduce this in our calculations, in agreement with Ref. 36, see Table III. These differences can most likely be attributed to the different pseudopotentials and technical details such as the used basis functions, see also the related discussion for the incipient ferroelectric material $SrTiO_3$.[38]

B. Polar phonon modes

In the following, the relative stability between the paraelectric state and a ferroelectric state with polarization along [001] will be discussed in the framework of the frozen phonon approach, cf. Refs. 13, 14, 16, and 37. For this purpose, the atoms are successively displaced along the eigenvector $\vec{Y}$ of the A_{2u} phonon mode and the total energy is monitored.

The eigenvector of the A_{2u} mode is fully determined by symmetry as it is the only polar mode along [001],[12] and a gradual shift of amplitude A along the eigenvector $\vec{Y}$ is thus given by the displacements $A\,(0,0,1)$ for Ti and $A\,(0,0,-m_{\mathrm{Ti}}/2m_{\mathrm{O}})$ for O atoms, respectively. Here, m_i represent the Ti and O masses.

While the paraelectric state is stable at the equilibrium lattice constants, the energy surface flattens around $A = 0$ for tensile [001] strain, or under an isotropic volume expansion. In both cases, the A_{2u} mode softens proportional to the imposed lattice modification, and two ferroelectric minima appear at a critical value of the lattice modification,[14,16,37] see left inset in Fig. 2. Although, so far, no such transition has been observed experimentally, a considerable modification of the A_{2u} mode frequency under external pressure has been measured.[2]

In order to discuss these ferroelectric trends in more detail, we expand the energy change per primitive cell during the polar displacement, $\Delta E(A)$, up to fourth-order with respect to $|A\,\vec{Y}|$,

$$\Delta E(A) = \frac{s}{2} A^2 |\vec{Y}|^2 + \kappa A^4 |\vec{Y}|^4 . \qquad (1)$$

For a qualitative discussion we use the stiffness s, which determines the curvature of the energy around the paraelectric state.

The stiffness is positive for a stable paraelectric state and changes its sign as the ferroelectric state becomes the energetic ground state. Figure 2 depicts the variation of the stiffness as a function of the Ti-O_{eq} bond length for the following modifications of the equilibrium crystal structure: (i) external pressure, (ii) isotropic lattice expansion, (iii) [001] strain, (iv) [$\bar{1}$10] strain, and (v) variation of the ratio between TiO_{eq} and TiO_{ap} bond lengths at constant volume by a variation of the internal parameter u. Here, for (i), all lattice parameters have been optimized at a given pressure, whereas neither the lattice

TABLE I. Bulk lattice parameters and Born charges Z^* (see Sec. III C for further details) of rutile TiO_2. Results obtained in the present work (top rows) are compared to literature data (bottom rows).

	a (Å)	c/a	u	$Z^*_{\parallel}$	$Z^*_{\perp}$	$Z^*_{[001]}$
GGA[a]	4.664	0.637	0.305	7.60	5.36	8.15
GGA[b]				7.25	. . .	7.73
LDA[16]	4.572	0.644	0.304	7.49	5.43	7.77
LDA[36]	4.535	0.641	0.303	7.27	5.25	7.32
GGA[36]	4.637	0.638	0.305	7.22	5.18	7.52
exp.[c]	4.587	0.644	0.305	. . .	. . .	. . .

[a]VASP.
[b]PWscf; structural parameters fitted to VASP results.
[c]4.2 K, Ref. 2.

TABLE II. Modification of the lattice parameters under external pressure P. Our values obtained with GGA potentials are opposed to values obtained with LDA potentials from Ref. 14, and experimental data are given for comparison. For each quantity, the calculated pressure dependence has been fitted by $f(P) = b_0 + b\,P$. The values for zero pressure, b_0 (left), and the slopes b, in units 10^3 GPa^{-1} for u and c/a, in units of 10^3 GPa^{-1}Å otherwise (right) are listed.

	b_0			b		
	LDA[14]	Here	Expt.[14]	LDA[14]	Here	Expt.[14]
a (Å)	4.55	4.66	4.59	−7.73	−9.1	−8.62
c (Å)	2.92	2.97	2.96	−2.41	−2.2	−2.14
u	0.304	0.305	. . .	−0.14	−0.2	. . .
c/a	0.64	0.64	0.64	0.56	0.8	0.79
TiO_{eq}(Å)	1.93	1.97	. . .	−1.70	−1.5	. . .
TiO_{ap}(Å)	1.96	2.01	. . .	−4.27	−5.4	. . .

TABLE III. Coefficients of total energy fits, Eq. (1), for atomic displacements along the A_{2u} mode and harmonic frequencies ω_0 in comparison with literature data. Top: external pressure; middle: tensile [001] strain; bottom: tensile [$\bar{1}$10] strain.

	Equation (1)		Harmonic frequencies			
	s (eV Å^{-12})	κ (eV Å^{-14})	PBE	LDA[14]	PBE[13]	LDA[37]
			ω_0(cm^{-1})			
Eq.	0.51	21.89	91	150	i 86	170
−2 GPa	0.14	21.36	47	100	. . .	150
−5 GPa	−0.58	21.71	i 97	. . .	. . .	. . .
1%	−0.50	20.74	i 90	130	. . .	. . .
2%	−1.36	17.85	i 148	100	. . .	. . .
5%	−4.00	15.29	i 254	i 125	. . .	. . .
2%	−0.76	. . .	i 110	. . .	. . .	. . .
5%	−2.30		i 192	. . .	. . .	

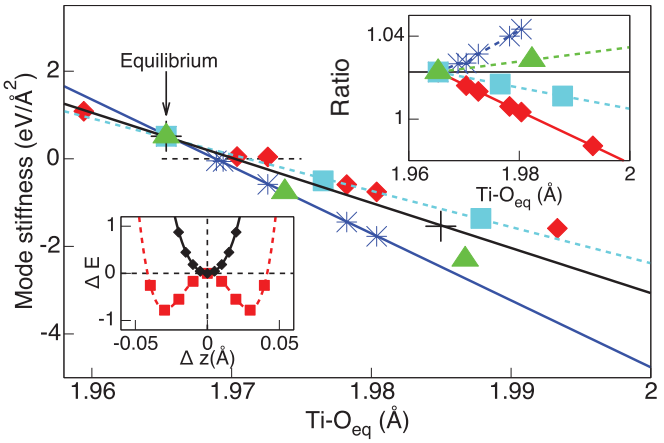

FIG. 2. (Color online) Stiffness s of the A_{2u} mode for different modifications of the equilibrium crystal structure: external pressure (blue, stars); u variation (red, diamonds); [001] strain (cyan, squares); [$\bar{1}$10] strain (green, triangles); and isotropic lattice expansion (black, crosses). (Left inset) Energy difference (meV/2 f.u.) for a static atomic displacement at the equilibrium lattice constants (black, diamonds) and under 1% tensile [001] strain (red, squares). Δz is the relative Ti-O displacement in [001] direction. (Right inset) Ratio of the Ti-O$_{ap}$ and Ti-O$_{eq}$ distances under the imposed lattice modifications.

vectors nor the internal parameter u have been optimized for all other cases.

It can be noticed that we obtain a stable ferroelectric state polarized along [001] for each tested lattice modification that enlarges the Ti-O$_{eq}$ bond, see Fig. 2. Even an artificial modification of the internal parameter u, which enlarges the Ti-O$_{eq}$ bonds and reduces the Ti-O$_{ap}$ distances without lattice expansion, stabilizes the ferroelectric phase.

For the case of [001] strain, it has been discussed in Ref. 14 that the large short-range repulsion, which appears under a relative displacement of the two sublattices, prevents a ferroelectric transition for the equilibrium structure, but that this contribution to the total energy decreases with increasing strain. Our systematic comparison of different lattice modifications further shows that it is sufficient to increase the Ti-O$_{eq}$ distance in order to stabilize the ferroelectric phase. Most likely, the relative displacements of these ions contribute most to the short-range repulsion as they correspond to the shortest Ti-O distance.

Even though all the various lattice modifications destabilize the paraelectric phase, the slopes of s as a function of the Ti-O$_{eq}$ bond length differ considerably for the different cases. Here, the differences in the Ti-O$_{ap}$ distances result in different contributions of these atomic pairs to the short-range repulsion. Additionally, the dipolar interaction is reduced as the ratio of the nearest and next-nearest Ti-O distances changes, see Sec. III C. As the dipole-dipole interaction is the second large contribution to the total energy that is affected by ferroelectric displacements,[39,40] its reduction reduces the ferroelectric trends considerably. Because of this, the slopes of s are correlated with the ratio of the two classes of Ti-O bond lengths, see right inset of Fig. 2. On the one hand, the configuration for which the atomic structure has been optimized under external pressure, shows the steepest s in Fig. 2, as an increase of the ratio of the TiO$_{ap}$ and TiO$_{eq}$ distances is superimposed to the lattice expansion, see Table II. On the other hand, s is notably flatter if the ratio of the two Ti-O distances decreases, e.g., under [001] strain or especially for a modification of u, which induces the largest decrease of the bond length ratio.

For a quantitative comparison of the obtained mode stiffness, the harmonic frequencies ω_0 can be obtained from Eq. (1),

$$\Delta E = \frac{\omega_0^2}{2} A^2 \left[2m_{\mathrm{Ti}} + 4m_{\mathrm{O}} \left(\frac{m_{\mathrm{Ti}}}{2m_{\mathrm{O}}} \right)^2 \right]. \qquad (2)$$

In this way, we obtain a frequency of the A_{2u} mode at the equilibrium structure, see Table III, which is within the spread of different theoretical estimates and below the experimental value of 173 cm^{-1}.[1] (See also the discussion in Sec. III A.) Apart from these quantitative differences, similar qualitative trends for the mode softening under a lattice modification (pressure and [001] strain) are obtained within the different theoretical studies.

In summary, a ferroelectric phase polarized along [001] can be stabilized for each tested expansion of the Ti-O$_{eq}$ bond. We will see in Sec. IV D that this result can qualitatively be transferred to the ferroelectric trends of the surface.

In the remainder of this section, we now discuss the actual displacement patterns of the atoms under different values of strain, which will be used as reference for the atomic displacements within the strained surfaces in Sec. IV D. For this purpose, we strain the bulk structure along the [001], respectively [$\bar{1}$10], direction and relax all atomic positions, whereas we do not consider a further relaxation of the lattice vectors perpendicular to the strain direction.[41]

If the atomic positions are optimized within the metastable paraelectric state, the internal parameter u slightly increases with strain (<1% for imposed strain of up to 5%), i.e., the ratio between the Ti-O$_{ap}$ and Ti-O$_{eq}$ distances increases, as the Ti-O$_{eq}$ distances are less sensitive towards strain or lattice expansion. This relaxation of the atomic positions is in agreement with previous work, e.g., Ref. 14.

If the paraelectric symmetry of the structure is lifted, we obtain polar displacements of the atoms, in agreement to the discussed softening of the polar modes under tensile strain, see Table IV. Polar displacements both along [001] and [$\bar{1}$10] directions lower the energy relative to the paraelectric state under 2% and 5% tensile strain, and the cases with polar displacements parallel to the strain direction are energetically most favorable for both strain orientations, cf. Ref 15.

We note that the amplitudes of the polar displacements are not the same for all Ti/O atoms in case of [$\bar{1}$10] strain. Two inequivalent Ti [Ti(1), Ti(2)] and O [O(1), O(2)] sublattices exist under such strain, as the equatorial Ti(2)-O(2) bonds are not modified while the imposed strain enlarges the apical Ti(2)-O bonds (the opposite holds for the Ti(1)-O distances), see Fig. 1(b). As a result, the short-range repulsion and thus the amplitudes of the atomic displacements differ for both atomic subclasses. Specifically, the displacements along [001] are larger for Ti(1)/O(1) than for Ti(2)/O(2) (and the other way round for the [$\bar{1}$10] displacements), cf. Refs. 17 and 18.

TABLE IV. Modification of the internal parameter u, polar displacements z of the Ti and O ions in Å, and the energy difference ΔE relative to the optimized paraelectric state in meV/atom for different imposed tensile strains. Ti(1)/O(1) corresponds to Ti-O_{ap} bonds along [110], Ti(2)/O(2) to Ti-O_{ap} bonds along [$\bar{1}$10], see Fig. 1(b). Top: ferroelectric state polarized along [001]; bottom: ferroelectric state polarized along [$\bar{1}$10].

Pol.	Strain	$u_{[\bar{1}10]}$	$u_{[110]}$	$z_{Ti(1)}$	$z_{Ti(2)}$	$z_{O(1)}$	$z_{O(2)}$	ΔE
[001]	$[001]_{+2\%}$	0.305		0.05		−0.05		−1
	$[001]_{+5\%}$	0.303		0.08		−0.13		−11
	$[\bar{1}10]_{+2\%}$	0.305		0.08	0.01	−0.02		−1
	$[\bar{1}10]_{+5\%}$	0.035	0.036	0.14	0.02	−0.04	−0.03	−4
[$\bar{1}$10]	$[001]_{+2\%}$	0.306		−0.02	−0.04	0.03	0.02	−0.1
	$[001]_{+5\%}$	0.307	0.306	−0.04	−0.07	0.07	0.04	−2
	$[\bar{1}10]_{+2\%}$	0.307	0.305	−0.04	−0.10	0.04	0.03	−2
	$[\bar{1}10]_{+5\%}$	0.311	0.307	−0.05	−0.19	0.09	0.03	−16

C. Born charges

As already mentioned previously, the energy difference between the paraelectric and the ferroelectric phase is often discussed in terms of a delicate balance between short-range repulsive forces and the long-range dipolar interaction, which favors the ferroelectric state.[39] It has been further shown for perovskites like $BaTiO_3$ that the dipolar interaction can counterbalance the short-range repulsion if an anomalous hybridization between the displaced ions lowers the energy during a ferroelectric transition.[40] The local chemical environment in TiO_2 is quite similar to the perovskite structure, with Ti^{4+} ions that are octahedrally coordinated with O^{2-} ions, and mostly ionic bonds with some covalent character. It is thus very likely that similar dynamic hybridization effects as in perovskites can also stabilize the ferroelectric state in strained rutile. Indeed, a Mulliken population analysis showed an increased Ti_d-O_p hybridization within the ferroelectric phase.[14]

To obtain a detailed understanding of this dynamic charge transfer, we make use of the dynamic Born effective charge,

$$Z^*_{ij,\kappa} = \frac{\Omega}{|e|}\frac{\partial P_i}{\partial r_{\kappa,j}}, \tag{3}$$

which describes the change in polarization P in direction i for a shift of atom κ in direction j. Here, Ω is the unit cell volume and $|e|$ the electronic charge. Due to the charge neutrality condition, $2\,Z^*_{\mathrm{Ti}} = -4\,Z^*_{\mathrm{O}}$, we can restrict the following discussion to Z^*_{Ti}. The effective charge tensor of Ti in rutile is diagonal in a [$\bar{1}$10], [001], [110] reference system, see Fig. 1(b), with the principal values $Z^*_{||}$, $Z^*_{[001]}$, and $Z^*_{\perp}$. Here, $Z^*_{||}$ is the dynamic charge along the apical bond, which is pointing along [110] respectively [$\bar{1}$10] for every second Ti atom, and $Z^*_{\perp}$ is the charge along the third perpendicular direction in each case.

In Table I, our values calculated with VASP and the values obtained form the shifts of the center of gravities of the maximally localized Wannier functions (MLWFs) based on PWscf calculations are compared to literature. Although the VASP results are slightly larger than all other values, due to the use of soft potentials, the qualitative trends are reproduced within both approaches.

It can be seen that, in particular, the [001]-component of the Born tensor, $Z^*_{[001]}$, is exceptionally large and of the same size as for ferroelectric materials ($BaTiO_3$: $Z^{Ti}_{[001]} = 7.3$).[42] Furthermore, the Born charge along the apical bond, $Z^*_{||}$, is also quite large and may stabilize a ferroelectric transition in [110]/[$\bar{1}$10] direction, whereas $Z^*_{\perp}$ is only moderately enhanced compared to the nominal ionic charge of +4.

As a first step towards the understanding of dipolar interactions at the rutile surface it is essential to understand in more detail the underlying mechanism for the exceptionally large Born effective charge of Ti^{4+} in bulk TiO_2, and how it is affected by different lattice modifications. These aspects will therefore be discussed in the remainder of this section.

Based on the constructed MLWFs, we decompose Z^*_{Ti} according to (see, e.g., Ref. 43)

$$Z^* = Z^*_{\mathrm{core}} + Z^*_{\mathrm{sc}} + Z^*_{\mathrm{val}}, \tag{4}$$

where $Z^*_{\mathrm{core}} = +12$ is the charge (in units of $|e|$) of the nucleus screened by the inner electrons, Z^*_{sc} the contribution of the Ti $3s$ and $3p$ semicore states, and Z^*_{val} is the contribution of the valence electrons. We find that the semicore contribution to $Z^*_{\mathrm{sc},[001]}$ ($Z^*_{\mathrm{sc},\parallel}$) differs only by −0.23 (−0.12) from the nominal value of −8. In contrast, large anomalous values appear for Z^*_{val}, which can be further decomposed into contributions of individual MLWFs, see Table V. Thereby, the 16 valence bands of TiO_2 with dominant O_{2s} and O_{2p} atomic character are represented by 16 MLWFs per unit cell, four orbitals per O ion. Starting from projections onto three atomic sp^2 hybrid orbitals, centered at each of the four different oxygen atoms and oriented towards the three surrounding Ti atoms, and one p orbital oriented perpendicular to the corresponding O-Ti_3 triangles [see Fig. 1(a)], we obtain three σ and one π-type orbital per oxygen as depicted in Fig. 3. We note that depending on the initial projection used for the spread minimization, different localized Wannier orbitals can be obtained, corresponding to various local minima of the total quadratic spread functional.

In agreement with the formal ionic Ti^{4+}-O^{2-} configuration, the centers of gravity of each MLWF are close to the central O atoms. Nevertheless, the mixed covalent-ionic character of the Ti-O bonds can clearly be seen from the d-character "tails" of the MLWFs at the Ti positions (see Fig. 3). This is consistent with the integrated projected density of states shown in Fig. 5,

TABLE V. Contributions of individual MLWFs (see Fig. 3) and total Z^*_{val}. O_{eq} (O_{ap}) correspond to MLWFs situated at equatorial (apical) oxygen atoms relative to the displaced Ti. Rows denoted "Eq." are calculated for the equilibrium structure, rows denoted "$u + 3\%$" are calculated for 3% increased internal parameter u. Top: $Z^*_{[001]}$; bottom: $Z^*_{||}$. In each case, the mean values for the corresponding orbitals are given.

		O_{eq}			O_{ap}			
		$p_\perp$	sp^2_{eq}	sp^2_{ap}	$p_\perp$	sp^2_{eq}	sp^2_{ap}	Z^*_{val}
$Z^*_{[001]}$	Eq.	0.48	0.30	0.04	−0.01	−0.01	−0.10	3.96
	$u + 3\%$	0.39	0.29	0.00	−0.03	−0.02	−0.08	3.26
$Z^*_{||}$	Eq.	−0.36	−0.04	0.06	0.48	0.23	0.29	3.38
	$u + 3\%$	−0.23	−0.08	0.05	0.53	0.27	0.31	4.20

which, for example, results in an occupation of about 0.6 electrons for the Ti d_{xy} atomic orbital, i.e., projection of the total density of states onto atomic orbitals within spheres of 1.32 Å for each Ti atom. Furthermore, the center of gravity of the σ-type MLWF along the shorter equatorial bond divides the bond with a ratio of 22:78, while the longer apical bond is divided with a ratio 20:80.

If the central Ti-atom is displaced along [001] ($[\bar{1}10]$), the Ti-O_{eq} (Ti-O_{ap}) distances are modified, and thus the covalent character of the corresponding bonds changes. This leads to a shift of the center of gravity of the MLWFs, which causes large and positive anomalous contributions to the Born effective charges, see Table V (we note that in the fully ionic case the valence contribution to the Ti Born effective charge would be identical to zero). Thus charge is dynamically transferred in and out of the Ti d orbitals. Similar to the case of the ferroelectric perovskite $BaTiO_3$,[43] the π-type orbitals ($p_\perp$) show the largest anomalous contributions to Z^*, underlining the large similarity between TiO_2 and the related ferroelectric perovskites.

In addition to these positive contributions, the MLWFs located at O_{ap} (O_{eq}), exhibit small negative contributions to $Z^*_{[001]}$ ($Z^*_{||}$). The corresponding Ti-O bond lengths do not change to first order in the displacements and thus no strong change in hybridization occurs. Instead, the charge contained in the "tails" of the corresponding MLWFs move with the Ti atom, leading to small negative contributions to Z^*. This effect is especially pronounced for the equatorial π-type orbital for a displacement of the Ti atom along $[\bar{1}10]$, thereby slightly reducing $Z^*_{||}$.

We note that a similar Wannier decomposition for the Born effective charge of the oxygen anion in rutile TiO_2 has been presented in Ref. 44. In agreement with our work, Cangiani *et al.* found the largest anomalous contributions to Z^*_{O} for the $p_\perp$-type orbitals. However, even though the total charges of Ti and O are related by the charge neutrality condition, the relation between individual orbital contributions is less straightforward, thus preventing a more detailed comparison.

Two important factors for the modification of the dipolar interaction at surfaces are atomic relaxation and structural distortions at the surface. In the following, we therefore consider different lattice modifications within the bulk system and investigate the resulting effect on the Born effective charges. Thereby, we are considering similar lattice modifications as in the previous section, i.e., a uniform lattice expansion, modification of the ratio of the Ti-O distances by u, and imposed strains in the [001] and $[\bar{1}10]$ directions, in each case without further relaxation of the other parameters. The results are depicted in Fig. 4.

A uniform lattice expansion leads to a small increase of both $Z^*_{[001]}$ and $Z^*_{||}$, while at the same time the static hybridization of the atoms is reduced, see Fig. 5. For all other distortions, the ratio of the Ti-O bond lengths is modified in addition to eventual changes in the volume. A variation of the internal parameter u in turn conserves the volume while increasing the equatorial bond distance and decreasing the apical bond distance. As seen in Fig. 5, this also changes the static hybridization. On one hand, the occupation of the Ti d and p states within the x-y plane increases with the largest gain for the d_{xy} orbital, which is oriented along the apical bond. On the other hand, the occupation of orbitals with lobes in [001] direction is reduced. Thus the Ti-O_{eq} (Ti-O_{ap}) hybridization decreases (increases), as do the weights of the corresponding tails in the MLWFs.

This change in the static hybridization seems to reduce the dynamic change in hybridization between the Ti and O_{eq} orbitals especially for the $p_\perp$ orbital. As a consequence, both the positive and negative contributions of this orbital to

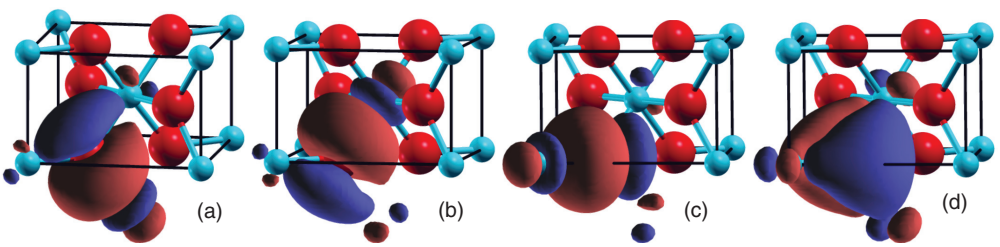

FIG. 3. (Color online) Maximally localized Wannier functions corresponding to (a) $sp^2_{\mathrm{eq,dn}}$, (b) $sp^2_{\mathrm{eq,up}}$, (c) sp^2_{ap}, and (d) $p_\perp$ orbitals.

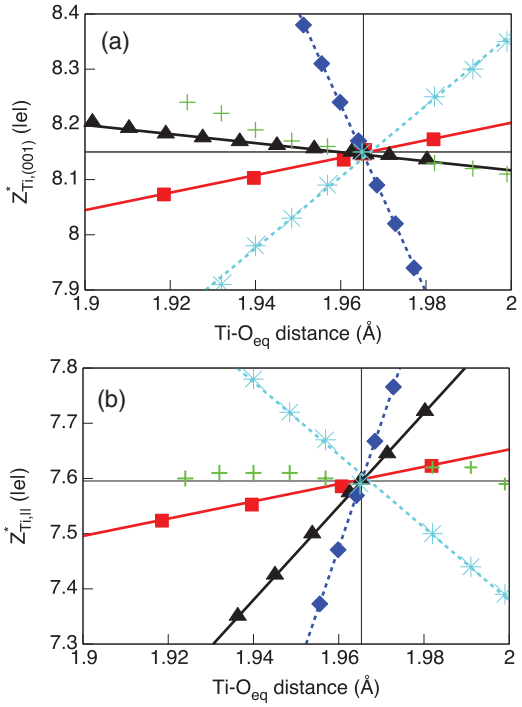

FIG. 4. (Color online) Change in the Ti Born charge $Z^*_{[001]}$ (a) and $Z^*_{||}$ (b) due to a modification of the equatorial Ti-O bond length by uniform lattice expansion (red, squares), modification of u (blue, diamonds), [001] strain (black, triangles), and [$\bar{1}$10] strain. For the case of [$\bar{1}$10] strain, the given Ti-O_{eq} distance corresponds to Ti(2) and the Born charges are depicted for both Ti(1) (cyan, stars) and Ti(2) (green, pluses).

$Z^*_{[001]}$ and $Z^*_{||}$, respectively, are reduced. Similarly, the reduced coupling of the sp^2_{ap} orbital with the equatorial Ti neighbor may explain the slight reduction of its contribution to $Z^*_{[001]}$. In contrast, the hybridization between the Ti atom and its apical neighbor increases for increased u, as do most of the negative and positive contributions of these orbitals to $Z^*_{[001]}$ and $Z^*_{||}$. In summary, a systematic reduction [increase] of the effective charge along [001] ([110]) occurs, see Fig. 4. For example, $Z^*_{val,[001]}$ ($Z^*_{val,||}$) decreases [increases] by 8% (24%) within the PWscf calculation for a u modification of $+3\%$. Thereby,

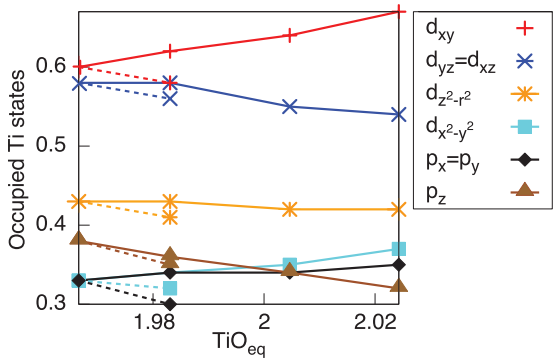

FIG. 5. (Color online) Orbitally resolved changes in the integrated valence density of Ti states due to a modification of the Ti-O bond lengths. Solid lines: modification of the internal parameter u. Dashed lines: uniform lattice expansion. x: [001], y: [010], z: [001].

the main reduction in $Z^*_{val,[001]}$ is due to a reduced anomalous contribution of the $p_\perp$ orbital at O_{eq}, whereas the increase of $Z^*_{val,||}$ is due to slightly enlarged contributions of $p_\perp$ and sp^2_{eq} at O_{ap} and a strong reduction of the negative contribution of $p_\perp$ at O_{eq}.

One may wonder, whether the absolute Ti-O_{ap} distance instead of the Ti-O bond ratio plays the major role for this modification of the static and dynamic hybridization. However, if the Ti-O_{eq} distances are modified for a fixed Ti-O_{ap} distance by a combination of isotropic expansion and a variation of u, the modification of $Z^*_{[001]}$ with the ratio of the Ti-O distances is equal to a variation of u.

As the change of the Ti-O bond length ratio is smaller in the case of [001] strain, the corresponding reduction (increase) of $Z^*_{[001]}$ ($Z^*_{val,||}$) is less pronounced. Similar to the modification of $Z^*_{||}$, the third principle value of the Born tensor, $Z^*_\perp$ slightly increases with a reduced ratio of the Ti-O distances. However, for small variations of the Ti-O distances, as they may appear at the surface, the absolute value of $Z^*_\perp$ is not significantly enhanced compared to the formal ionic charge, and thus no considerable influence on the ferroelectric trends has to be expected from this modification.

For [$\bar{1}$10] strain, the ratio of Ti-O bonds corresponding to Ti(2) is modified analogously to the case of [001] strain, and indeed the corresponding decrease of $Z^*_{[001]}$ is identical to [001] strain for small strain values, see Fig. 4(a). In contrast, the apical bond length increases for Ti(1) while the equatorial distance stays constant, and thus $Z^*_{[001]}$ increases for this Ti atom. Furthermore, while $Z^*_{||}$ is nearly independent of the equatorial bond distance for Ti(2) under [$\bar{1}$10] strain, $Z^*_{||}$ decreases drastically for Ti(1) with the corresponding expansion of the apical bond.

In summary, the largest individual contributions to the anomalous Born effective charges in rutile stem from the large dynamic charge transfer along Ti-O π bonds. Additionally, the static Ti-O hybridization, which depends strongly on the ratio of both Ti-O distances, leads to considerable modifications of the effective charges. The resulting modification of the dipolar interaction has a considerable influence on the ferroelectric properties of the rutile surface, as we will see in Sec. IV C. Furthermore, we find large effective charges, which are stable against small lattice distortions, as they may appear at the rutile surface.

IV. (110) SURFACE

For the investigation of the ferroelectric trends of the rutile surface, we use two different approaches. After summarizing the structural relaxations at the surface we first briefly discuss the ferroelectric trends for a free film of seven monolayers (ML), whereas in Secs. IV C and IV D, we model the clamping of the film due to an idealized substrate by fixing two bottom layers to paraelectric, respectively ferroelectric positions of the bulk material under different strain conditions (see Table IV).

As can be seen in Fig. 6, the (110) surface consists of Ti-O_p layers with bridging oxygen (O_b) atoms between these layers. The surface Ti atoms are alternately fivefold coordinated (Ti_{5c}) and sixfold coordinated (Ti_{6c}). We note that we use the nomenclature Ti_{6c} (Ti_{5c}) not only for the atoms in the first surface layer, but also for the corresponding Ti atoms below.

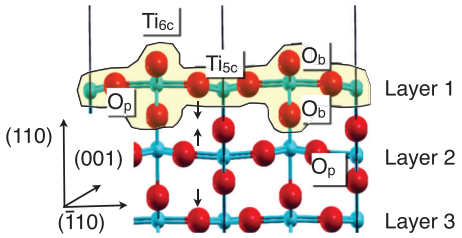

FIG. 6. (Color online) Atomic structure of the topmost layers of the rutile (110) surface. Light cyan: Ti, red: O. Black arrows: interlayer distance oscillation.

A. Surface relaxation

The calculated atomic structure of the paraelectric films is very similar for free and clamped films and thus we restrict the discussion to the structural relaxation of the clamped film. The corresponding results are summarized in Table VI. Even though the rutile (110) surface is nonpolar and stable without reconstruction, the atomic structure is significantly modified at the surface. It has been discussed in literature that the atomic structure converges only slowly with film thickness.[7,8,10] However, we obtain only modifications of the interatomic distances smaller than 0.01 Å if the film thickness is increased to 9 layers. Additionally, our obtained structural relaxation at the surface agrees well with previous results in literature.[7,8,10]

Most notably, the outermost Ti_{5c} and O_b atoms in the first surface layer relax inwards and reduce their distance towards the underlying apical and equatorial neighbors by 9%, respectively 6.1% (6.6%), in our calculations (in Ref. 8). In contrast, the next deeper Ti-O bonds along the surface normal are enlarged by 3.6%, respectively 7.1%, for the equatorial Ti_{5c}-O_b and Ti_{6c}-O_b pairs. This alternating modification of the Ti-O bonds reaches several angstroms deep into the surface, cf. Refs. 7 and 10.

Apart from this oscillation of the Ti-O distances, a small surface buckling appears, as Ti_{5c} atoms and bridging O atoms (O_b) relax inwards whereas Ti_{6c} and O atoms within Ti-O planes (O_p) relax outwards, see Fig. 6. It has been debated in literature[23] whether an alike polar surface relaxation of $SrTiO_3$ can be interpreted as ferroelectric relaxation along the surface normal. However, this relaxation does not break the symmetry of the ideal surface and thus cannot be interpreted as a ferroelectric transition, nor can there exist two switchable states.[21]

In summary, the Ti-O bonds along the surface normal are considerably modified and show a large anisotropy for each Ti atom, whereas the bond lengths perpendicular to the surface normal are very close to their bulk values, see Table VI.

B. Free surface

Due to the strong symmetry lowering at the surface, the ferroelectric phonon modes of the bulk are no longer eigenmodes of the system. Most notably, the Ti-O_{eq} distances vary between 1.83 and 2.11 Å, see Table VI. This means that the short-range repulsion during a ferroelectric shift is locally very different, and one may expect different amplitudes of polar displacements in each layer. As a result of this, a polar displacement of the whole slab along the bulk A_{2u} mode (i.e., with the same relative displacement between Ti and O in all layers) is energetically very unfavorable. The stiffness of such a displacement increases by a factor of ten in comparison to bulk.

However, if all atomic positions are optimized after such a static displacement along the bulk A_{2u} mode, small polar displacements persist within the film. For instance, the total energy of the paraelectric system is lowered by 3 meV/cell if mainly the Ti_{6c} atom in layer 3 is displaced by 0.07 Å along [001] against its surrounding O octahedra, resulting in a dipole moment of 0.8 $|e|$ Å [determined with Eq. (5)]. For this Ti atom, the enlarged short-range repulsion due to the shrink of two equatorial bonds of 2% can be compensated, as the apical bond is nearly conserved and the two other equatorial bonds increase by about 3%. A ferroelectric configuration becomes even more favorable if small polar displacements in [$\bar{1}$10] direction are superimposed to the displacement along [001], and we obtain an energy gain of 5 meV/atom relative to the paraelectric surface.

Although these small energy well depths will most likely be overcome by thermal or even quantum fluctuations, the presence of such polar surface states confirms the strong

TABLE VI. Ti-O bond lengths (Å) within the three outermost layers of the rutile (110) surface within the paraelectric state (see Fig. 6) with and without strain. The bulk distances refer to the optimized paraelectric structure with corresponding strain. Left columns: Ti_{6c}: sixfold coordinated Ti atoms in the surface and Ti rows below. Right columns: Ti_{5c}: fivefold coordinated Ti atoms in the surface and Ti rows below. A single entry corresponds to Ti-O neighbors in plane, while each Ti atom possesses different distances towards its inner/outer O_b neighbors.

		bulk		3	2	1		3	2	1
Eq.	Ti-O_{eq}	1.97	Ti_{6c}	2.02/1.92	1.98	2.11/1.85	Ti_{5c}	1.96	1.90/2.04	1.96
	Ti-O_{ap}	2.01		2.02	2.21/1.87	2.06		1.92/2.13	2.00	1.83/-
$[001]_{+2\%}$	TiO_{eq}	1.96	Ti_{6c}	2.04/1.93	2.00	2.13/1.85	Ti_{5c}	1.98	1.91/2.07	1.98
	TiO_{ap}	2.06		2.03	2.20/1.86	2.06		1.92/2.13	2.00	1.83/-
$[001]_{+5\%}$	TiO_{eq}	1.97	Ti_{6c}	2.07/1.94	2.04	2.16/1.87	Ti_{5c}	2.01	1.92/2.10	2.01
	TiO_{eq}	2.01		2.03	2.18/1.84	2.07		1.90/2.11	2.00	1.81/-
$[\bar{1}10]_{+2\%}$	TiO_{eq}	1.96	Ti_{6c}	2.00/1.92	2.00	2.09/1.85	Ti_{5c}	1.97	1.90/2.03	1.97
	TiO_{ap}	2.06		2.07	2.19/1.88	2.11		1.94/2.12	2.04	1.85/-
$[\bar{1}10]_{+5\%}$	TiO_{eq}	1.97	Ti_{6c}	1.99/1.92	2.01	2.08/1.85	Ti_{5c}	1.98	1.90/2.01	1.98
	TiO_{ap}	2.01		2.14	2.18/1.89	2.19		1.96/2.12	2.11	1.86/-

ferroelectric trend at the rutile surface, which is comparable to the $SrTiO_3$ surface.[21] In addition, these polar displacement patterns demonstrate the large modification of the polar phonon mode at the surface. Thus, in order to investigate the ferroelectric trends of the free surface using the frozen phonon approach (similar to what has been done for the bulk material, see Sec. III B), it would be necessary to calculate mode eigenvectors for the strained films. However, since the determination of surface phonon modes is computational very demanding, we will follow a slightly different approach in order to investigate the ferroelectric trends of the surface in the remainder of this paper.

C. Clamped surfaces

We use the atomic structure of the bulk material within the paraelectric or ferroelectric phases, see Table IV, as starting point and fix two bottom layers to these bulk positions. This setup corresponds to a clamping of the bottom layers to an underlying substrate. By using this procedure, the amplitude of the displacements within the upper layers can account for the local atomic arrangement of the surface, and thus will approach the real eigenstate of the system.

To quantify the local polar displacements, we use the total dipole moment p_i per Ti_2O_4 layer i:

$$\vec{p}_i = \sum_j Z^{*j}_{\Delta\vec{r}} \Delta\vec{r}_j, \tag{5}$$

where Z^{*j} is the Born charge of atom j along $\vec{r}$, and $\Delta\vec{r}_j$ is the shift with respect to the paraelectric reference configuration of each atom j within layer i.

As mentioned previously, the surface properties of TiO_2 converge only slowly with film thickness. This is especially important for electronic properties such as the band gap.[7,10] Furthermore, the clamping of one surface of the slab could induce artificial electronic surface states, which could then modify the ferroelectric trends. To address this issue, Fig. 7 shows the layer-resolved total density of states (DOS) corresponding to the Ti atoms. Indeed, surface states appear within the band gap at the fixed bottom surface, see Fig. 7(a). However, these states decay rapidly with increasing distance from the bottom layer and do not significantly influence the electronic structure of the free top surface. In addition, the DOS obtained here is in qualitative agreement with the electronic structure obtained in previous investigations.[7] The largest modification of the electronic structure in comparison to the bulk material is a slight narrowing of the band gap, due to a small shift of the unoccupied d states of the Ti_{5c} atoms.

As discussed by Bredow *et al.*,[7] the hybridization between Ti and O states, which are oriented along the surface normal, oscillates with the surface distance. These surface-induced modifications of the hybridization are correlated with the reduced (enlarged) Ti-O distances at the surface, see Sec. IV A. As we showed in Sec. III C, small changes in the Ti-O arrangement and hybridization can have considerable influence on the ferroelectric characteristics. Because of this, it is essential to have a detailed understanding of the character of the Ti-O bonding in the vicinity of the surface in order to make predictions on the ferroelectric trends. For this purpose, we decompose the valence states of the surface slab into MLWFs, see Fig. 8. We note that in order to obtain qualitative trends at a reasonable computational effort, this decomposition has been performed for a free film with a thickness of only three monolayers.

It can be seen from Figs. 8(a) and 8(b) that the MLWFs with sp^2_{ap} and $p_\perp$ character, which belong to the topmost O_b atom, are considerably modified in comparison to bulk. For both orbitals, the Ti atom in the apical position is missing at the surface, and the centers of gravity shift towards the Ti_{6c} atom below, see Fig. 8(c). Thus the covalent character of this bond increases. Similarly, the hybridization of the undercoordinated Ti_{5c} surface atom and the O_b atom below is enlarged. Overall, an alternating increase and decrease of the Ti-O hybridization appears along the surface normal, and the amplitude of this oscillation decreases with the surface distance, fully consistent with the changes in the corresponding bond lengths. Thereby, the strongest shifts correspond to the centers of gravity of the $p_\perp$-type MLWFs, which, as shown in Sec. III C, also exhibit the largest individual contributions to the bulk Born effective charges. Furthermore, we also found in Sec. III C that a modification of this $p_\perp$ orbital also leads to a considerable modification of the dynamic charges, and thus an oscillating modification of the dynamic charges can be expected at the rutile surface.

In order to verify this conclusion, we now discuss the modifications of the Born effective charges at the (110) surface

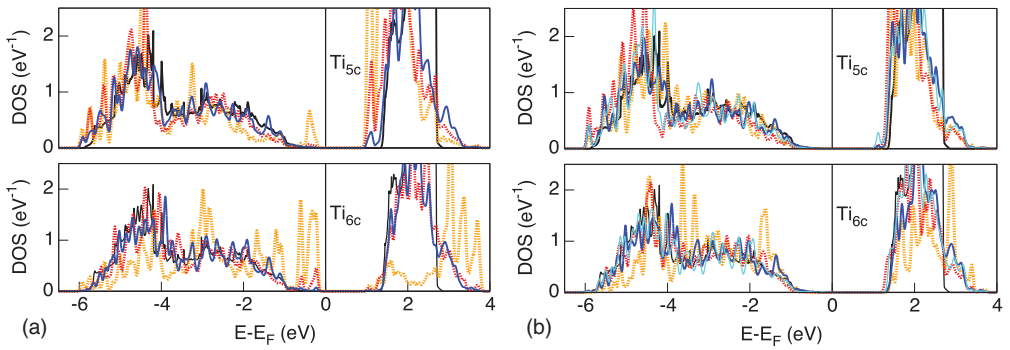

FIG. 7. (Color online) Layer resolved Ti density of states: first layer (yellow, light, dotted); second layer (red, darker, dotted); third layer (blue, dark, solid line); fourth layer (cyan, light, solid line), and bulk value as thin black lines. (a) The numbering starts at the fixed bottom of the film. (b) The numbering of layers starts at the relaxed surface.

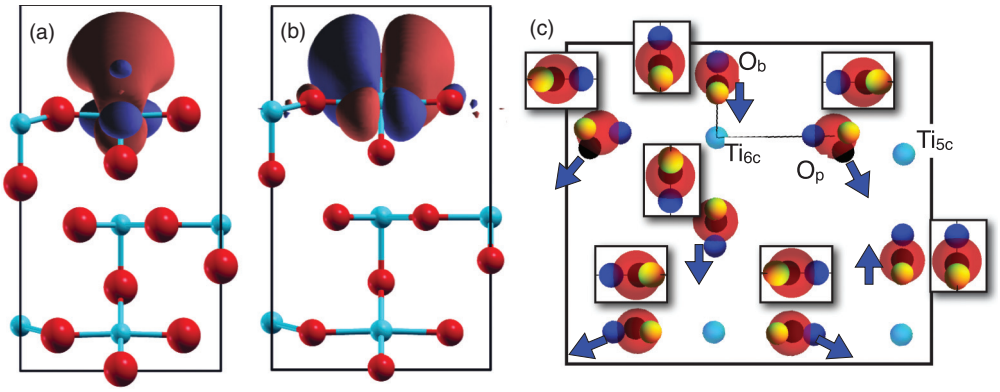

FIG. 8. (Color online) (a) and (b) MLWFs of the topmost O_b atom: (a) sp^2_{ap} and (b) $p\perp$ orbitals. (c) Centers of gravity of the MLWFs close to the surface. Light, yellow spheres: sp^2_{eq}; dark, blue spheres: sp^2_{ap}; black spheres: $p_\perp$ orbital. The bulk distribution of the MLWF centers is given as reference within the small boxes. Arrows mark the overall shift of charge at the surface relative to the bulk structure.

in more detail. Figure 9 shows the Born charges along [001] and [$\bar{1}$10] for each class of atoms. (Due to the reduced symmetry at the surface, small off-diagonal elements of the Born tensor appear, which we neglect in our discussion.) We only consider cases with polarization within the surface plane, in order to avoid complications due to the strong depolarizing fields perpendicular to the surface. The Born charges are calculated both for the structurally relaxed as well as for the unrelaxed surface configuration.

For a detailed discussion of dipolar interactions along [$\bar{1}$10], one has to keep in mind that $Z^*_{||}$ and $Z^*_\perp$ are alternating in this direction. While all apical bonds are aligned along [110] for O_b ($Z^*_{[\bar{1}10]} = Z^*_\perp$), they are aligned within the surface for the O_p atoms ($Z^*_{[\bar{1}10]} = Z^*_{||}$). For the Ti atoms, $Z^*_{||}$ and $Z^*_\perp$ are alternating in each layer, see Figs. 9(d)–9(f).

It is apparent from Fig. 9 that even if atomic relaxations are neglected, the dynamic charges are strongly modified within the topmost layers. In particular, $Z^*_{[001]}$ of the outermost Ti_{6c} [(c)] and O_b atoms [(a)] is significantly enlarged in comparison

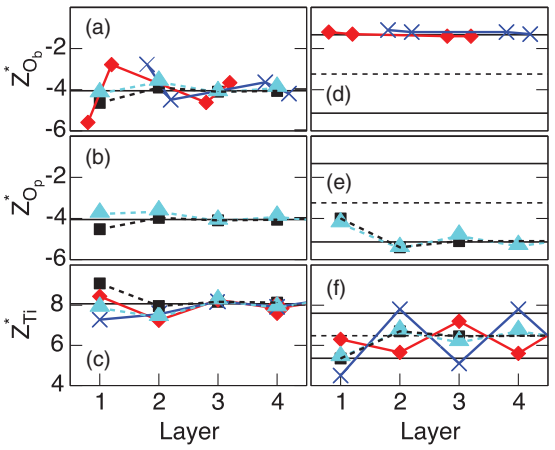

FIG. 9. (Color online) Values of (a)–(c) $Z^*_{[001]}$, (d)–(f) $Z^*_{\bar{1}10}$: $Z^*_{||}$, and $Z^*_\perp$ (solid lines). (a) and (d): O_b (b) and (e): O_p, (c) and (f): Ti; Ti_{6c} atoms and the corresponding O_{eq} atoms (red, diamonds); Ti_{5c} and the corresponding O_{eq} atoms (blue, cross); mean value (cyan, triangles); mean value of the unrelaxed cell (black, squares). Lines are a guide to the eye only.

to bulk, while the corresponding charges within the topmost Ti_{5c} [(c)] atom and its equatorial O_p [(b)] neighbors are slightly reduced. Also, the dynamic charges along [$\bar{1}$10] are reduced within the topmost surface layer, as the mean value $Z^*_{[\bar{1}10]}$ of the Ti atoms [(f)] and $Z^*_{[\bar{1}10]}$ of O_p [(e)] atoms are slightly reduced.

If we account for atomic relaxations, the alternating strong and weak Ti-O bonds appear along the surface normal, as discussed above. Especially, the modification of the Ti-O_{eq} bonds has a considerable effect on the Born charges along [001]. Simultaneous with the modification of the equatorial Ti-O_b bonds, $Z^*_{[001]}$ of these O_b atoms oscillates, i.e., the dynamic charge transfer increases (decreases), if the corresponding Ti-O_{eq} bonds are strengthened (weakened), while the amplitude of this oscillation decreases with increasing distance from the surface (as does the oscillation of the bond strength). This is fully consistent with the reduction (increase) of $Z^*_{[001]}$ for a reduced (enlarged) Ti-O_{eq} static hybridization of the bulk material, see Sec. III C.

We note that the charge neutrality condition does not hold for each layer under the reduced symmetry at the surface, and as a result, about 0.2 electrons are transferred from the dynamic charges of layer 1 to the ones of layer 2. In particular, the Born charges of the uppermost Ti_{5c} atom and the Ti_{6c} atom in layer 2 are not balanced by their equatorial neighbors. For these Ti atoms, the Ti-O_{ap} bonds along the surface normal are reduced to 1.83 Å, respectively, 1.87 Å and are thus shorter than the bulk Ti-O_{eq} bonds. Because of this, the Born charge in layer 1 is slightly reduced. Besides the direct surface, the mean Born charges per layer of Ti, O_p, and O_b atoms oscillate with a slight increase in odd layers.

The mean values of $Z^*_{[\bar{1}10]}$ also oscillate with the surface distance for Ti and O_p atoms, see Figs. 9(e)–9(f), but, the Born charge is enlarged within even layers opposite to $Z^*_{[001]}$. This behavior is consistent with the opposite trends of $Z^*_{[001]}$ and $Z^*_{||}$ for different modification of the Ti-O bond ratio and hybridization in the bulk. $Z^*_\perp$ of the O_b atoms is nearly constant while $Z^*_\perp$ of Ti_{6c} (Ti_{5c}) increase (decrease) marginally. As the Ti-O bonds within the surface planes are modified to a smaller extent, the oscillations of $Z^*_{||}$ of O_p atoms are only very minor. Besides this, $Z^*_{||}$ of Ti_{6c} (Ti_{5c}) is reduced (enlarged) in all layers

and a dynamic charge transfer of about 0.2 $|e|$ appears from layers with odd numbers to layers with even numbers.

Furthermore, the in-plane modification of the Ti-O_{eq} bonds is much smaller, as is the change of the dynamic charge transfer within the planes. Overall, besides the discussed modifications of the Born effective charges, the large anomalous dynamic charges along [001] and [$\bar{1}$10] found in the bulk system are retained at the (110) surface of rutile. Therefore a similar tendency towards a ferroelectric distortions as in the bulk material can also be expected at the surface.

D. Strained surface

In the following, we present our results on polar atomic distortions of the clamped surface. For the unstrained film, we tested the stability of polar distortions along [001] by a displacement of 0.1 Å along the polar A_{2u} bulk mode of the 2 clamped bottom layers, cf. Sec. III B. As the upper layers are fully relaxed, this setup corresponds to the clamping of the TiO_2 film to a ferroelectric substrate. Although, small polar displacements are stable with respect to the paraelectric configuration in layers 3–5, the amplitude of these polar displacements decays with the distance towards the polar layers and thus no stable polarization is obtained directly at the surface, see Fig. 10(a). This decline of the polarization shows that the ferroelectric state is not stable within the unstrained film although a large polarizability is present. Furthermore, the decay of the polar distortions is even more pronounced if compressive [001] strain is imposed. This indicates that a ferroelectric distortion might be stabilized by a systematic expansion of the Ti-O distances, cf. discussion of the bulk case in Sec III B.

Indeed, polar distortions along [001] or [$\bar{1}$10] are stable within the TiO_2 surface for 2% uniaxial tensile strain, see Fig. 10. Additionally, the short-range repulsion is further reduced for an increasing tensile strain and thus the local dipole moments increase systematically if we impose an uniaxial expansion of 5%.

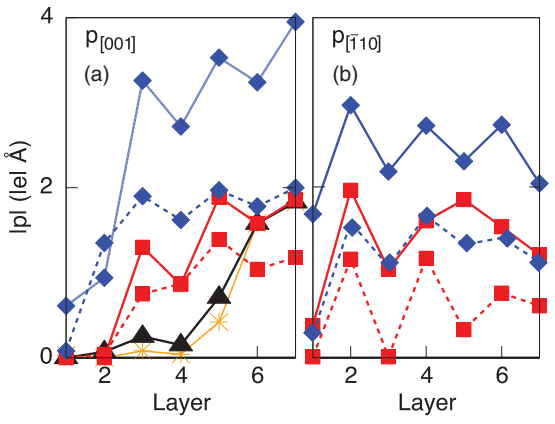

FIG. 10. (Color online) Layer-resolved dipole moments under tensile uniaxial strain. (a) $|\vec{p}_{[001]}|$ (b) $|\vec{p}_{[\bar{1}10]}|$. Solid (dotted) lines correspond to strain parallel (perpendicular) to the polarization. 2% compressive strain (yellow, stars); no strain (black, crosses); 2% tensile strain (red, squares); and 5% tensile strain (blue, diamonds). In all cases, polar distortions perpendicular to the polarization direction of the substrate are prevented by the imposed symmetry.

TABLE VII. Energy gain relative to the corresponding paraelectric case (meV/2 f.u. surface cell) of the different polar surface configurations, see text. The bottom layers are fixed to the polar state along [001] ([$\bar{1}$10]) in the first (second) row. Only in-plane displacements parallel to the bottom polarization are allowed. (The upper layers are fully relaxed resulting in local dipole moments along [001] and [$\bar{1}$10].)

	[001] strain		[$\bar{1}$10] strain	
Bottom layers	2%	5%	2%	5%
[001] polarized	18 (25)	262 (275)	3 (48)	111 (518)
[$\bar{1}$10] polarized	−1	48 (128)	28	525

Table VII lists the energy gain for the different polar displacements in comparison to the strained paraelectric films. In agreement with the bulk system, both polar states along [001] and [$\bar{1}$10] are energetically more favorable than the paraelectric state and thus two stable ferroelectric states exist. Obviously, the polar distortions parallel to the imposed strain are energetically most stable. But, in agreement to the strained bulk, the paraelectric state is also unstable against a polar distortion in the direction perpendicular to the strain, see Table IV. Only for 2% [001] strain, the paraelectric state is more favorable than the ferroelectric state perpendicular to the strain direction.

For the obtained dipole patterns in Fig. 10, we constrained the atomic optimization and enforced the local dipoles to point parallel to the fixed bottom layer. In contrast, if all atomic degrees of freedom are optimized without such constraint, local dipoles both along and perpendicular to the polarization of the fixed bottom layer form, see Fig. 11. For the polar states along [001], the system obviously gains energy, if superimposed polar distortions along [$\bar{1}$10] are formed, Table VII. The energies for polar distortions in both directions are given in brackets. The modification of the local dipoles is even more pronounced under tensile strain along [$\bar{1}$10]. Polar distortions along [001] can be stabilized under such

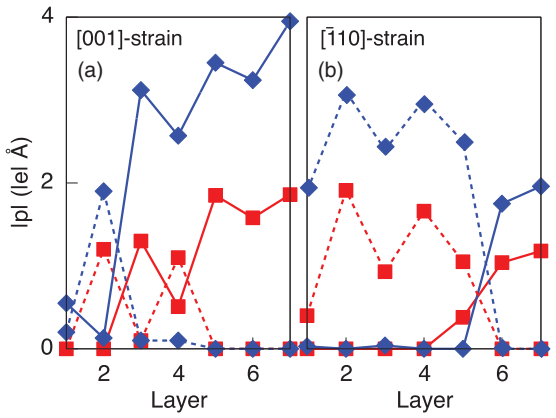

FIG. 11. (Color online) Layer-resolved dipole moments under tensile uniaxial strain for an optimization of the atomic structure without imposed symmetry. The substrate layers have been fixed to the corresponding polar states along (001). Solid lines: $|p_{[001]}|$, dashed lines: $|p_{[\bar{1}10]}|$; 2% strain (red, squares); 5% strain (blue, diamonds); (a) [001]-strain; (b) [$\bar{1}$10]-strain.

strain if the symmetry of the system is fixed, which could possibly be achieved by an external electric field. Despite this, polar distortions parallel to the strain direction are much more favorable and are even stable on top of a ferroelectric substrate polarized along [001], see Fig. 11(b).

We now discuss the observed layer-dependent variations of the local dipoles. In all cases, the local dipole moments in [001] ($[\bar{1}10]$) direction are enlarged in layers with an odd (even) number. Besides this, the local polarization in [001] direction slightly decreases towards the surface and is quenched within the first layer for $[\bar{1}10]$ strain or 2% expansive [001] strain. For the local polarization along $[\bar{1}10]$, no systematic decay of the polarization towards the surface is obtained, although the polarization in the first layer is considerably reduced for all kinds of strain.

The different Ti-O distances and thus the local variations of the short-range repulsion have a large influence on the obtained dipole patterns, see discussions in Secs. III B and IV B. The Ti-O distances at the surface and thus the short-range repulsion oscillates with the distance form the surface. Additionally, the tensile strain further modifies the spatial variation of the Ti-O distances. First of all, the Ti-O_{eq} distances within the Ti-O_p planes increase systematically with both kinds of tensile strain, see Table VI. In addition, the apical distances in-plane increase with $[\bar{1}10]$ strain whilst they are not modified by strain along [001]. Because of this, the short-range repulsion that builds up during a polar shift between Ti atoms and their O_p neighbors in [001] and $[\bar{1}10]$ direction is reduced considerably and thus polar distortions are stabilized by tensile strain.

As the tensile in-plane strain enlarges the atomic volume, a shrink of the atomic distances along the surface normal is very likely. Indeed, the Ti-Ti interlayer distances decrease for tensile [001] strain. In contrast to this, no unique reduction of the interlayer distances can be found for tensile $[\bar{1}10]$ strain.

Additionally, for the Ti-O bonds oriented perpendicular to the surface, the discussed strengthening (weakening) of the bond has a significant impact on the atomic relaxation under imposed strain. On the one hand, the strengthened bonds are rather insensitive to tensile strain. In particular, the distance between the Ti_{6c} atom in layer 1 and the outer O_b atom is not modified by 2% [001] or $[\bar{1}10]$ strains and shows an expansion of only 1% under 5% [001] strain. As a consequence, a polar displacement of this Ti_{6c} atom relative to the surrounding atoms along [001] is not stable, even at 5% expansive strain in either direction. On the other hand, the length of the less covalent bonds increases (decreases) systematically under expansive [001] ($[\bar{1}10]$) strain. Because of this, the asymmetry of the Ti-O bond lengths along the surface normal increases (decreases) slightly with the imposed [001] ($[\bar{1}10]$) strain for each Ti atom.

Besides the modified short-range repulsion, the dynamic charges at the rutile surface oscillate with the distance from the surface, see Fig. 9. Consequently, the local dipole moments show the same trends with maximal (minimal) local dipole moments along [001] in odd (even) layers and the other way around for polarization along $[\bar{1}10]$. Here, the magnitude of Z^* has a direct influence on the local dipole moments, see Eq. (5). Also, the local variation of the dipolar interaction leads to a modulation of the atomic displacements.

Thus the considerable difference between $Z^*_{||}$ and $Z^*_{\perp}$ leads to different amplitudes of the $[\bar{1}10]$ displacements of Ti_{5c} and Ti_{6c} atoms in each layer. For example, the apical bond of the Ti_{6c} atoms in the first layer is aligned along $[\bar{1}10]$ and thus the displacement of this atom against the surrounding oxygen octahedra is a factor of two larger than those of the Ti_{5c} atom within the same layer. Analogously, the displacement of the Ti_{5c} atom in each even layer is a factor of two larger than the displacements of the corresponding Ti_{6c} atom. Additionally, $Z^*_{||}$ is considerably larger within the even layers, as are the amplitudes of the polar distortions. Similarly, the reduction of $\vec{p}_{[001]}$ in the layers with an even number is due to a reduced displacement of the Ti_{6c} atoms within these layers, which is correlated with the reduced dipolar interaction along [001] for these atoms.

Both $Z^*_{[001]}$ and $Z^*_{[\bar{1}10]}$ are slightly modified under tensile strain, see Table VIII. For example, $Z^*_{[001]}$ of the O_b atoms increases (decreases) for the strengthened (weakened) bonds, while the Born charge of the O_p atoms is insensitive towards such strain. As a consequence, the oscillation of the dipolar interaction is slightly enlarged in comparison to the equilibrium lattice constant. For $[\bar{1}10]$ strain, $Z^*_{[001]}$ of all O_p and Ti atoms

TABLE VIII. Born charges ($|e|$) within the paraelectric phase of the rutile (110) surface calculated with VASP for different values of uniaxial [001] and $[\bar{1}10]$ strains. For the Ti_{6c}/Ti_{5c} atoms and the Ti atoms below, respectively, the O_p and O_b atoms, the Born charges for the first free surface layers are given, see Fig. 6. Top: $Z^*_{[001]}$. Bottom: $Z^*_{[\bar{1}10]}$.

	Ti_{6c}			Ti_{5c}			O_p			O_b		
Strain	1	2	3	1	2	3	1	2	3	1	2	3
No strain	8.4	7.3	8.3	7.3	7.6	8.2	−3.8	−3.7	−4.1	−5.6/−2.8	−2.8/−4.5	−4.6/−3.7
$[001]_{+2\%}$	8.6	7.2	8.3	7.3	7.6	8.2	−3.8	−3.7	−4.1	−5.8/−2.7	−2.7/−4.6	−4.7/−3.6
$[001]_{+5\%}$	8.7	7.1	8.4	7.2	7.6	8.1	−3.8	−3.6	−4.1	−6.1/−2.6	−2.5/−4.7	−4.8/−3.5
$[\bar{1}10]_{+2\%}$	8.6	7.3	8.4	7.4	7.7	8.3	−3.8	−3.7	−4.2	−5.7/−2.9	−2.9/−4.5	−4.7/−3.8
$[\bar{1}10]_{+5\%}$	8.9	7.5	8.7	7.6	8.0	8.4	−3.9	−3.8	−4.2	−5.7/−3.1	−3.1/−4.6	−4.7/−4.0
No strain	6.3	5.7	7.2	4.5	7.8	5.1	−4.3	−5.5	−4.9	−1.2/−1.3	−1.1/−1.2	−1.4/−1.4
$[001]_{+2\%}$	6.4	5.7	7.4	4.6	7.9	5.1	−4.4	−5.6	−5.0	−1.1/−1.3	−1.1/−1.2	−1.4/−1.4
$[001]_{+5\%}$	6.7	5.9	7.6	4.7	8.0	5.3	−4.6	−5.6	−5.2	−1.2/−1.3	−1.1/−1.2	−1.4/−1.4
$[\bar{1}10]_{+2\%}$	6.1	5.7	7.0	4.4	7.8	4.9	−4.1	−5.5	−4.8	−1.1/−1.3	−1.1/−1.2	−1.4/−1.4
$[\bar{1}10]_{+5\%}$	5.9	5.7	6.7	4.2	7.6	4.8	−4.0	−5.3	−4.6	−1.2/−1.3	−1.1/−1.2	−1.4/−1.3

is enlarged and thus the magnitude of the $Z^*_{[001]}$ oscillation is reduced. Simultaneously, the layer-wise oscillation of $\vec{p}_{[001]}$ is smaller for $[\bar{1}10]$ strain.

V. CONCLUSIONS AND OUTLOOK

We have investigated the ferroelectric trends of the incipient ferroelectric material TiO_2 rutile by means of first-principles calculations. Similar to the well-known ferroelectric perovskites, rutile possesses anomalously large dynamic charges, which is one key factor for the stabilization of a ferroelectric phase.

We could show that this strong dynamic charge transfer is mainly mediated by π-type O-Ti hybrid orbitals. Furthermore, this dynamic charge transfer is considerably modified by changing the ratio of the equatorial and apical Ti-O bond lengths. Nevertheless, a large dynamic charge transfer along the [001] direction and along the apical Ti-O bonds is preserved under small variations of the lattice as they may appear at strained surfaces. Indeed, the Born charges in both directions are quite stable at the (110) surface of rutile, even if one imposes an uniaxial tensile strain in the surface planes. Only small oscillations of the dipolar interaction appear with the surface distance. Here, the dipolar interaction along [001] is slightly enhanced within every second Ti-O layer starting from the topmost layer, while the dipolar interaction along $[\bar{1}10]$ is slightly larger in the odd layers.

Although, the material possesses such a large dynamic charge transfer, no ferroelectric transition appears, as the short-range repulsion, which builds up during a polar displacement is too large for the undistorted material. In agreement with previous theoretical studies, we have shown that a ferroelectric transition of the bulk material can be enforced by lattice expansion or by uniaxial tensile strain. In both cases, the enlarged Ti-O distances reduce the short-range repulsion during a polar displacement. Additionally, we could show that a ferroelectric state polarized along [001] can be stabilized by all modifications of the lattice that enlarge the nearest Ti-O distance, even if the apical Ti-O distance shrinks during the lattice modification. For uniaxial strain along [001] and $[\bar{1}10]$, stable ferroelectric states can be found and for both kinds of strain, the polar displacement along the strain direction is most favorable.

Most notably, the stabilization of two ferroelectric states, one polarized along [001] and one along $[\bar{1}10]$ can be transferred from the bulk material to the rutile (110) surface. We thus find large local dipole moments already for 2% tensile strain in both [001] and $[\bar{1}10]$ directions. Although the ferroelectric trends and the obtained local dipole moments may be slightly overestimated within our theoretical approach, we find a successive increase of the local dipole moments for increasing strain. Therefore we predict that a ferroelectric state can be stabilized for experimentally accessible tensile strains, and that the resulting electric dipoles persist even in the atomic layers at or immediately below the surface. On the other hand, for compressive strain, no stabilization of a ferroelectric phase is possible at the rutile surface, in agreement with the corresponding bulk material.

ACKNOWLEDGMENTS

A. Grünebohm and P. Entel acknowledge financial support by the Deutsche Forschungsgemeinschaft (SFB 445, SPP1599) and C. Ederer by Science Foundation Ireland (SFI-07/YI1/I1051). The authors thank the John von Neumann Institute of Computing (NIC) and the Jülich Supercomputing Center (JSC) as well as the Center of Computational Science and Simulation (CCSS) of the University of Duisburg-Essen for computing time. Some calculations have also been performed at the Trinity Centre for High Performance Computing (TCHPC).

*anna@thp.uni-due.de

†Previous address: School of Physics, Trinity College, Dublin 2, Ireland.

[1] J. G. Traylor, H. G. Smith, R. M. Nicklow, and M. K. Wilkinson, Phys. Rev. B **3**, 3457 (1971).

[2] G. A. Samara and P. S. Peercy, Phys. Rev. B **7**, 1131 (1973).

[3] R. A. Parker, Phys. Rev. **124**, 1719 (1961).

[4] K. Siefering and G. L. Griffin, J. Electrochem. Soc. **137**, 1206 (1990).

[5] B. O'Regan and M. Grätzel, Nature (London) **353**, 737 (1991).

[6] K. Schierbaum, X. Wei-Xing, S. Fischer, and W. Göpel, *Adsorption on Ordered Surfaces of Ionic Solids and Thin films* (Springer, Berlin, 1993).

[7] T. Bredow, L. Giordano, F. Cinquini, and G. Pacchioni, Phys. Rev. B **70**, 035419 (2004).

[8] S. P. Bates, G. Kresse, and M. J. Gillan, Surf. Sci. **385**, 386 (1997).

[9] U. Diebold, Surf. Sci. Rep. **48**, 53 (2003).

[10] P. Murugan, V. Kumar, and Y. Kawazoe, Phys. Rev. B **73**, 075401 (2006).

[11] M. Ramamoorthy, D. Vanderbilt, and R. D. King-Smith, Phys. Rev. B **49**, 16721 (1994).

[12] C. Lee, P. Ghosez, and X. Gonze, Phys. Rev. B **50**, 13379 (1994).

[13] B. Montanari and N. M. Harrison, Chem. Phys. Lett. **364**, 528 (2002).

[14] B. Montanari and N. M. Harrison, J. Phys.: Condens. Matter **16**, 273 (2004).

[15] N. Li-Hong, L. Yong, R. Zhao-Hui, S. Chen-Lu, and H. Gao-Rong, Chin. Phys. B **20**, 106102 (2011).

[16] P. D. Mitev, K. Hermansson, B. Montanari, and K. Refson, Phys. Rev. B **81**, 134303 (2010).

[17] A. Grünebohm, C. Ederer, and P. Entel, Phys. Rev. B **84**, 132105 (2011).

[18] A. Grünebohm, M. Siewert, P. Entel, and C. Ederer, Ferroelectrics **429**, 1 (2012).

[19] K. Rabe, C. Ahn, and J.-M. Triscone, *Physics of Ferroelectrics-A Modern Perspective* (Springer, Berlin, Heidelberg, 2007).

[20] V. Ravikumar, D. Wolf, and V. P. Dravid, Phys. Rev. Lett. **74**, 960 (1995).

[21] J. Padilla and D. Vanderbilt, Surf. Sci. **418**, 64 (1998).

[22] B. Meyer, J. Padilla, and D. Vanderbilt, Faraday Discuss. **114**, 395 (1999).

[23]N. Bickel, G. Schmidt, K. Heinz, and K. Müller, Phys. Rev. Lett. **62**, 2009 (1989).
[24]J. H. Haeni, P. Irvin, W. Chang, R. Uecker, P. Reiche, Y. L. Li, S. Choudhury, W. Tian, M. E. Hawley, B. Craigo *et al.*, Nature (London) **430**, 758 (2004).
[25]W. Kohn and L. J. Sham, Phys. Rev. **140**, A1133 (1965).
[26]G. Kresse and J. Furthmüller, Phys. Rev. B **54**, 11169 (1996).
[27]P. E. Blöchl, Phys. Rev. B **50**, 17953 (1994).
[28]M. Gajdoš, K. Hummer, G. Kresse, J. Furthmüller, and F. Bechstedt, Phys. Rev. B **73**, 045112 (2006).
[29]J. P. Perdew, K. Burke, and M. Ernzerhof, Phys. Rev. Lett. **77**, 3865 (1996).
[30]J. Muscat, N. M. Harrison, and G. Thornton, Phys. Rev. B **59**, 2320 (1999).
[31]J. Serrano, F. J. Manjón, A. H. Romero, A. Ivanov, M. Cardona, R. Lauck, A. Bosak, and M. Krisch, Phys. Rev. B **81**, 174304 (2010).
[32]H. J. Monkhorst and J. D. Pack, Phys. Rev. B **13**, 5188 (1976).
[33]P. Giannozzi *et al.*, J. Phys.: Condens. Matter **21**, 395502 (2009).
[34]A. A. Mostofi, J. R. Yates, Y.-S. Lee, I. S. D. Vanderbilt, and N. Marzari, Comput. Phys. Commun. **178**, 685 (2008).
[35]N. Marzari and D. Vanderbilt, Phys. Rev. B **56**, 12847 (1997).
[36]E. Shojaee and M. R. Mohammadizadeh, J. Phys.: Condens. Matter **22**, 015401 (2009).
[37]Y. Liu, L. Ni, Z. Ren, G. Xu, C. Song, and G. Han, J. Phys.: Condens. Matter **21**, 275901 (2009).
[38]R. A. Evarestov, E. Blokhin, D. Gryaznov, E. A. Kotomin, and J. Maier, Phys. Rev. B **83**, 134108 (2011).
[39]W. Cochran, Adv. Phys. **9**, 387 (1960).
[40]P. Ghosez, X. Gonze, and J.-P. Michenaud, Europhys. Lett. **33**, 713 (1996).
[41]We note that an optimization of the lattice vector in [110] direction under 2% expansion in $[\bar{1}10]/[001]$ direction results in a decrease of only 0.2%/0.4 % for the paraelectric state.
[42]P. Ghosez, X. Gonze, P. Lambin, and J.-P. Michenaud, Phys. Rev. B **51**, 6765 (1995).
[43]C. Ederer, T. Harris, and R. Kováčik, Phys. Rev. B **83**, 054110 (2011).
[44]G. Cangiani, A. Baldereschi, M. Posternak, and H. Krakauer, Phys. Rev. B **69**, 121101 (2004).